

¹ Seasonality in Ocean Mesoscale Turbulence in a High Resolution
² Global Climate Model

³ Takaya Uchida¹, Ryan Abernathey^{1,2}

⁴ 1: Department of Earth and Environmental Sciences, Columbia University in the City of New York

⁵ 2: Lamont-Doherty Earth Observatory

⁶ Shafer Smith³

⁷ 3: Center for Atmosphere Ocean Science, New York University

⁸ 205A Oceanography 61 Route 9W - PO Box 1000 Palisades, NY 10964-8000, US

⁹ **Abstract**

We examine the seasonal cycle of upper-ocean mesoscale turbulence in a high resolution CESM climate simulation. The ocean model component (POP) has 0.1° degree resolution, mesoscale resolving at low and middle latitudes. Seasonally and regionally resolved wavenumber power spectra are calculated for sea-surface kinetic energy (KE), sea-surface temperature (SST) and sea-surface salinity (SSS). Although the spectral slopes themselves are not very informative (due to the strong presence of dissipation), the KE spectra consistently show higher power at small scales during winter throughout the ocean. Potential hypotheses for the seasonality are investigated. Linear quasigeostrophic stability analysis suggests that the seasonality originates in the submesoscale range (on the scales of the mixed-layer Rossby wavelength) and seasonally varying mixed-layer instability is proposed as the driver. The ability of this climate model, which is not considered submesoscale resolving, to produce mixed layer instability demonstrates the ubiquity and robustness of this process for modulating upper ocean energy.

¹⁰ **Keywords:** Parallel Ocean Program, mesoscale turbulence, seasonality, quasi-geostrophy,
¹¹ wavenumber spectra, linear stability analysis

¹² **1 . Introduction**

¹³ Mesoscale turbulence is ubiquitous in the ocean and has significant impacts on the large-
¹⁴ scale ocean circulation and its interaction with the climate (e.g. *Jayne and Marotzke*, 2002;
¹⁵ *Volkov et al.*, 2008; *Lévy et al.*, 2010; *Dong et al.*, 2014). Ocean currents are most energetic in

16 the mesoscale range, on the order of tens to a few hundred kilometers. Mesoscale turbulence is
17 well described by quasi-geostrophic (QG) models (*Rhines*, 1979; *Held et al.*, 1995), in which
18 enstrophy and energy conservation lead to the inverse cascade of energy from small to large
19 scales (*Charney*, 1971). Mesoscale turbulence is powered by baroclinic instability of the large-
20 scale flow (*Gill et al.*, 1974; *Smith*, 2007). Below the mesoscale lies the submesoscale, which
21 feeds off of the available potential energy in the mesoscale fronts, particularly in the mixed
22 layer (*Boccaletti et al.*, 2007). It is an open debate to what extent submesoscale flows are
23 governed by QG dynamics (*McWilliams*, 2016).

24 QG turbulence theory makes predictions for energy cascades and power law scaling in the
25 isotropic wavenumber spectrum. Hence, taking a long-term mean of the wavenumber spectra
26 of sea-surface height (SSH) and kinetic energy (KE) fields has been a powerful method to
27 characterize the physical difference between mesoscale and submesoscale turbulence in model
28 outputs and observations (e.g. *Stammer*, 1997; *Thomas et al.*, 2008; *Capet et al.*, 2008; *Xu and*
29 *Fu*, 2012). *Xu and Fu* (2012) made a global estimate of two-dimensional (2D) along-track
30 spectral slopes of SSH observed by altimetry on satellites, *Jason-1* and *Jason-2*. They found
31 that the SSH spectral slopes are generally steeper than k^{-2} and in regions of high eddy activity;
32 the spectral slopes had values between k^{-5} and $k^{-11/3}$ which were consistent with predictions
33 by QG (*Charney*, 1971) and surface-QG (SQG) theory (*Held et al.*, 1995; *Lapeyre and Klein*,
34 2006) respectively.

35 As our understanding of turbulence has progressed, however, time dependence, especially
36 seasonal variability, has been recognized as a key factor in understanding the KE spectra, par-
37 ticularly in the submesoscale range (*Mensa et al.*, 2013; *Sasaki et al.*, 2014; *Qiu et al.*, 2014;
38 *Brannigan et al.*, 2015; *Callies et al.*, 2015; *McCaffrey et al.*, 2015; *Rocha et al.*, 2016b,a).
39 There have been at least four main hypotheses proposed to explain seasonality in the 10-100
40 km range; (i) variation in the interior baroclinic instability (BCI) due to seasonality in the verti-
41 cal shear of the full-depth background state (*Qiu et al.*, 2014), (ii) variation in the mixed-layer
42 (ML) BCI due to seasonality in ML stratification, depth and vertical shear in the mixed layer
43 (*Callies et al.*, 2016; *Qiu et al.*, 2014; *Boccaletti et al.*, 2007), (iii) variation in frontogenesis
44 (FG) due to seasonality in lateral strain and convergence in horizontal density gradients (*Mensa*

45 *et al.*, 2013) and (iv) variation in internal gravity wave energy due to seasonality in upper ocean
46 stratification (*Rocha et al.*, 2016b). Most of the studies cited above are regional, and there is
47 no strong consensus about the relative roles of these mechanisms on a global scale. Our study
48 attempts to resolve this question.

49 In this paper, we investigate seasonal variability in wavenumber power spectra for eddy
50 kinetic energy (EKE), sea-surface temperature (SST), and sea-surface salinity (SSS) in an ocean
51 model. Many of these fields are observable through remote sensing, albeit with significant noise
52 and sampling issues, and a global climate model (GCM) study provides a useful test bed for
53 future work on satellite observations. Additionally, because of its resolution and dynamical
54 limitations, the analysis of such a GCM serves as an experiment into the mechanisms which
55 can drive seasonality. The ocean model is an 0.1° -resolution configuration of the Parallel Ocean
56 Program (POP) model, run within a fully coupled climate model (the Community Earth System
57 Model; CESM) (henceforth we shall refer this model run as the POP simulation). To our
58 knowledge, the seasonality of ocean turbulence has not been examined in this new category of
59 model on a global scale. According to the criteria of *Hallberg* (2013), this configuration ranges
60 from mesoscale-resolving at low latitudes to mesoscale-permitting at high latitudes. Although
61 this is fine resolution for a climate model, it is coarse compared to recent numerical studies
62 of submesoscale seasonality, some of which have used a spatial resolution of 1 km or even
63 higher (*Mensa et al.*, 2013; *Sasaki et al.*, 2014; *Gula et al.*, 2014; *Brannigan et al.*, 2015;
64 *Rocha et al.*, 2016a,b). Considering that it is still impractically computationally expensive
65 to run submesoscale-resolving global climate models, our study provides insights into how
66 mesoscale-resolving models reproduce seasonal variations. We present evidence that the POP
67 simulation may still resolve some aspects of ML BCI.

68 The paper is organized as follows. In section 2, we give a brief description of the POP
69 model. The results of spectral analysis and comparison of the spectral slopes among seasons are
70 shown in section 3. In section 4 we test various hypotheses for the drivers of EKE seasonality,
71 and we summarize our results in section 5. The details of our spectral analysis and linear
72 stability analysis are given in the appendix.

73 **2 . Description of the numerical model**

74 The ocean simulation we examine is a part of the fully-coupled global simulation using the
75 CESM described in *Small et al.* (2014), which was run under present-day greenhouse gas condi-
76 tions for 100 years, similar to *McClean et al.* (2011). The POP model, which is the ocean com-
77 ponent, is a level-coordinate ocean general circulation model that solves the three-dimensional
78 primitive equations for ocean dynamics. The hydrostatic and Boussinesq approximations are
79 prescribed, and the model employs a B-grid (scalars at cell centers, vectors at cell corners) for
80 the horizontal discretization scheme. The time discretization scheme uses a three-time-level
81 second-order-accurate modified leap-frog scheme for stepping forward in time. The diffusive
82 terms are evaluated using a forward step.

83 Subgrid scale horizontal mixing is parameterized using biharmonic diffusivity and viscos-
84 ity, with the coefficients spatially varying with the equatorial values of $A_H = -3.0 \times 10^9 \text{ m}^4/\text{s}$
85 and $A_M = -2.7 \times 10^{10} \text{ m}^4/\text{s}$ respectively. The vertical diffusion depends on the K-profile
86 parameterization (KPP) of *Large et al.* (1994). Further details about the discretization and ad-
87 vection schemes of the primitive equations and parameterization methods are described in the
88 Parallel Ocean Program Reference Manual (*Smith et al.*, 2010). The horizontal grid spacing in
89 the POP simulation is approximately 0.1° in latitude/longitude. Each component of the cou-
90 pled model exchanges information at different time intervals, with the atmosphere, sea ice, and
91 land models coupling every time step (15 min), and the ocean every 6 hours. The simulation
92 outputs at the ocean surface were saved as daily averages, while interior information was saved
93 as monthly average. The available model output constrains the scope of our analysis; since the
94 monthly averages are too smooth to provide meaningful wavenumber spectra, we focus on the
95 surface. More details of the model setup can be found in *Small et al.* (2014).

96 A video of the sea surface temperature in the Kuroshio region is available online at <https://vimeo.com/channels/oceandynamics/99933667>. This video clearly shows the
97 formation of secondary instabilities on the fronts of mesoscale eddies; this process appears to be
98 much more active in winter, when mixed layers are deep. Although the spatial resolution of this
99 model (0.1°) is not considered submesoscale resolving, the video suggests that submesoscale
100 mixed-layer instability may still be at work. This visualization provided the motivation for our

102 subsequent quantitative analysis of seasonality.

103 3 . Spectral Analysis of the Velocity and Tracer Fields

104 Spectral analysis provides a practical way to characterize the scale-dependent variance in
105 the simulation. In this section we present the calculation of horizontal isotropic wavenumber
106 spectra of the velocity and tracer fields. To resolve regional variability, we split up the domain
107 over the globe into 10° latitude-longitude boxes and calculate the spectra for each subdomain.
108 For every daily-averaged field in each subdomain, we remove the spatial mean by subtracting
109 the bi-linear trend derived from the least-square plane fit of the horizontal fields and apply a 2D
110 Hanning window. In deriving the wavenumber spectrum, we approximate a local tangent plane
111 in Cartesian geometry and take the 2D Fourier transform of the anomaly fields. We then take
112 the average over the azimuthal direction to create an isotropic spectrum. We sample the spatial
113 fields every 13 days, which is approximately the temporal decorrelation time. For the purposes
114 of calculating the error, each individual spectrum is therefore treated as an independent real-
115 ization of the process. Using 41 years of data, we have 1135 individual spectra. Numerical
116 implementation and normalization of the spectra is discussed in Appendix A.2 and A.3.

117 3 .1. *Snapshots of tracer fields and example of spectra*

118 The annual mean spectral slopes are shown in Fig. 1. In most regions, the spectral slopes
119 are in the range predicted by QG theory but some regions have slopes steeper than -3, which is
120 likely due to the biharmonic diffusion discussed later on. Before moving to the global picture,
121 however, we first examine the details of the spatial and spectral fields in a few energetic regions
122 of the ocean (Kuroshio, Gulf Stream, and ACC). The location of the regions is shown in Fig. 1.
123 (Additional regions are presented in Appendix A.1).

124 Figure 2 shows instantaneous spatially detrended fields of relative vorticity (ζ), buoyancy
125 ($b = -g\delta\rho/\rho_0$; $\delta\rho = \rho - \rho_0$, $\rho_0 \equiv 1025 \text{ kg/m}^3$), SST and SSS on March 1 and September 1
126 (representative of winter and summer) in model year 46. We see the spatial fields have more
127 small scale features and secondary instabilities forming on the peripheries of mesoscale eddies
128 on March 1, particularly in the SST and SSS field.

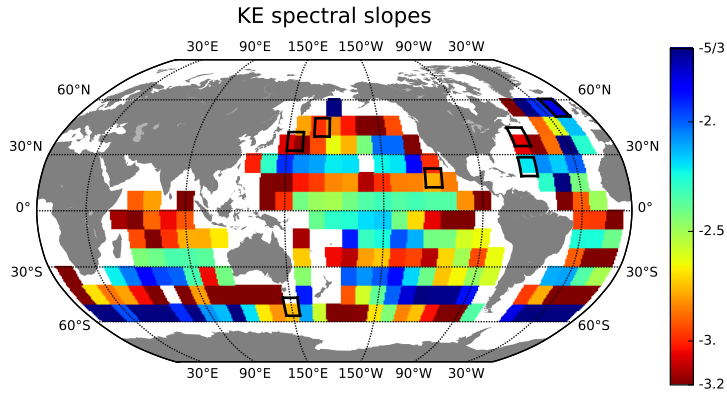


Figure 1: Annual mean of spectral slopes at scales above 200km (5×10^{-3} cpkm). The black boxes indicate the seven regions (Kuroshio, north of Kuroshio, east Pacific, Gulf Stream, Sargasso Sea, northeast Atlantic and the ACC) we consider in depth.

129 The seasonally-averaged isotropic wavenumber spectra (B) of EKE, SST, and SSS are
 130 shown (Fig. 3) for the Kuroshio, Gulf Stream and ACC regions. Boreal winter is defined as
 131 January, February and March (JFM), spring as April, May and June (AMJ), summer as July,
 132 August and September (JAS) and autumn as October, November and December (OND). (The
 133 spectra for the other four regions are shown in Appendix A.1.) Comparing the KE spectra for
 134 each season, the spring spectra have the highest energy in the lower mesoscale range (between
 135 50km and 100km, i.e. $10^{-2} - 2 \times 10^{-2}$ cpkm) while autumn has the lowest energy. At the
 136 smallest scales, the KE spectra have most power in winter and least power in summer. As for
 137 SST and SSS, there is not a significant difference in slopes but the variance is higher across
 138 scales during the winter for SST. The seasonality of SSS is opposite from SST in some regions.
 139

140 3.2. Seasonality in spectral power and slopes

141 Theoretical models of ocean mesoscale turbulence predict spectral slopes in the inertial
 142 range (Charney, 1971; Held *et al.*, 1995) and many previous studies have used spectral slopes
 143 to characterize ocean turbulence in observations and numerical models (e.g. Stammer, 1997;
 144 Thomas *et al.*, 2008; Capet *et al.*, 2008; Xu and Fu, 2011, 2012). We follow suit and calcu-
 145 late the spectral slopes by fitting a straight line to the log-log spectrum using the least-square
 146 method. Due to limited spatial resolution and the influence of sub-grid dissipation, the slope fit
 147 is extremely sensitive to the choice of wavenumber range.

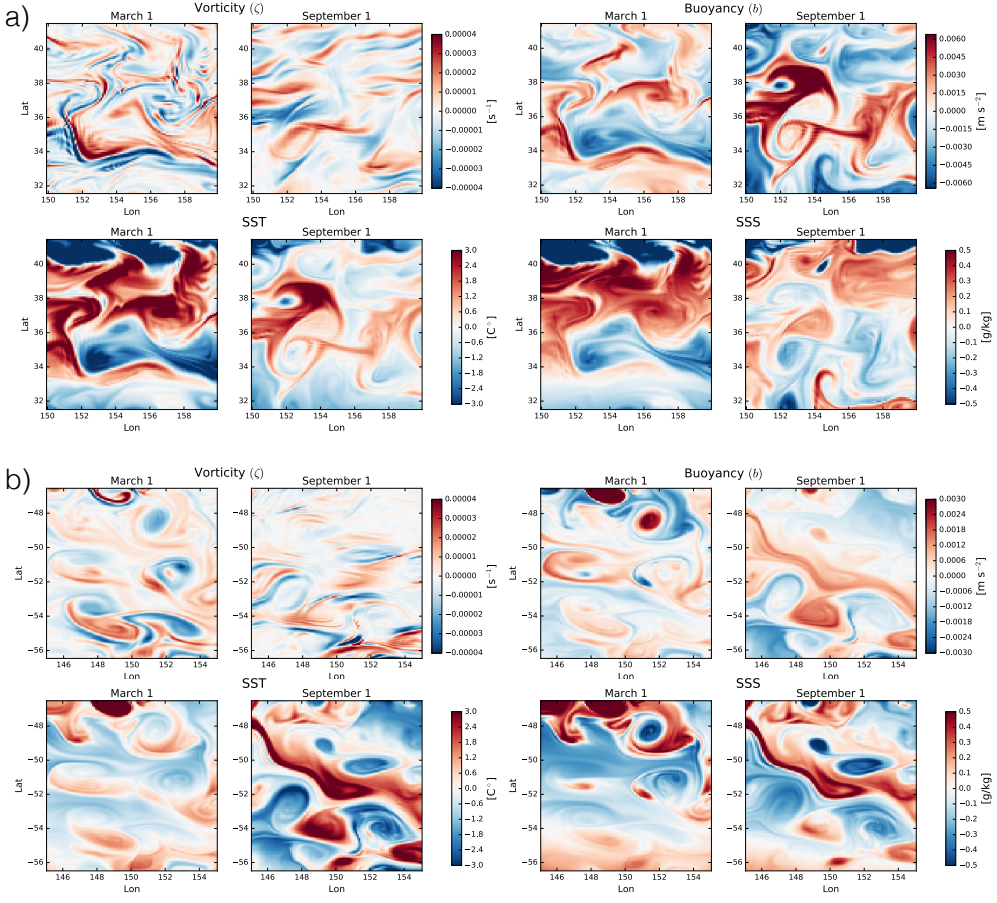


Figure 2: Snapshot of the anomaly fields of vorticity (ζ), buoyancy (b), SST and SSS on March 1 and September 1 in (a) the Kuroshio (lon: 150.0E~160.0E, lat: 31.5N~41.5N) and (b) ACC (lon: 145.0E~155.0E, lat: 56.5S~46.5S) region.

148 We address dissipation by explicitly calculating the momentum tendency due to lateral
 149 biharmonic diffusion in the spectral domain (see Appendix A.4 for details). We define the
 150 "dissipation range" as the wavenumber range above which 80% of dissipation occurs. From
 151 Fig. 3, we see that the dissipation range is broad and extends into the mesoscale range. This is
 152 likely the main cause for the steepening of the spectral slopes towards high wavenumbers. The
 153 influence of dissipation means it is problematic to compare the actual values of slopes in this
 154 range with turbulent inertial range theory. The dissipation is broad band so there is no likely
 155 inertial range at any scale. The slope fit is therefore performed on scales between 200 km and
 156 250 km (i.e. $4 \times 10^{-3} - 5 \times 10^{-3}$ cpkm), which is outside of the dissipation range globally.
 157 Figure 4 shows the resulting slope difference between summer / autumn and winter / spring.
 158 We see the seasonal contrast between spring (AMJ) and autumn (OND) is the strongest and
 159 most coherent, which is consistent to what we saw in the regional spectra (Fig. 3).

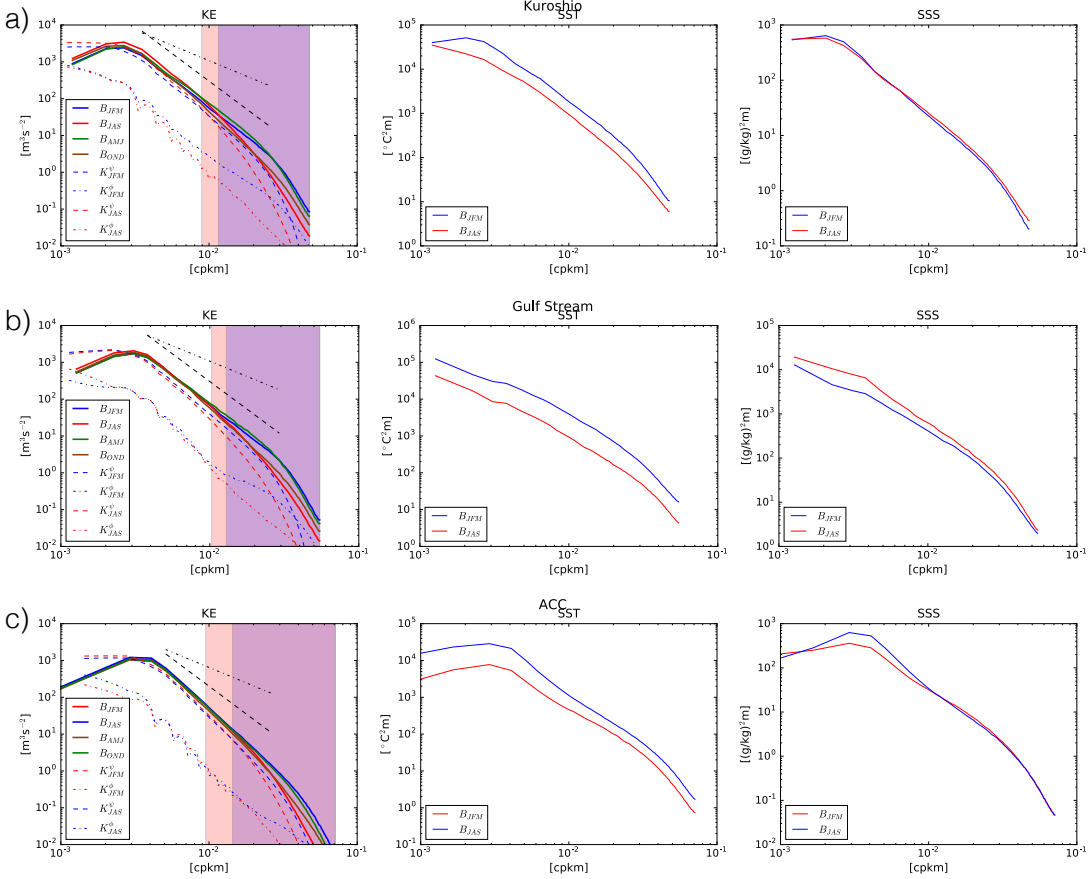


Figure 3: Seasonally-averaged spectra in eddy active regions: (a) Kuroshio, (b) Gulf Stream, and (c) ACC. The shading shows the dissipation range defined as where 80% of the dissipation due to bihamonic diffusion occurs (blue: winter, red: summer). The black dashed and dotted lines show the spectral slope of -3 and -5/3 respectively. The colored dashed and dotted spectra show the rotational and divergent component respectively. The 95% confidence intervals were thinner than the lines used to plot the spectra and so are not shown.

The slope analysis neglects the broad dissipation range, but interesting behavior still occurs within the dissipation range. To quantify the energy at the smallest scales, we perform a band average in the spectral range representing scales below 30km (3.3×10^{-2} cpkm); the resulting seasonal difference in small scale KE is shown in Fig. 5. A strong seasonal cycle is clearly present in both hemispheres.

The tracer (SST and SSS) spectral slopes did not show any significant seasonality; however, as evident in Fig. 3, variance changes strongly across seasons at all scales. In Fig. 6, we show the seasonality in the tracer variance on scales smaller than 30km (3.3×10^{-2} cpkm), the same spatial range in which we compared the KE energy seasonality. We observe that SST has more variance during winter at the smallest scales, while SSS has reversed seasonality.

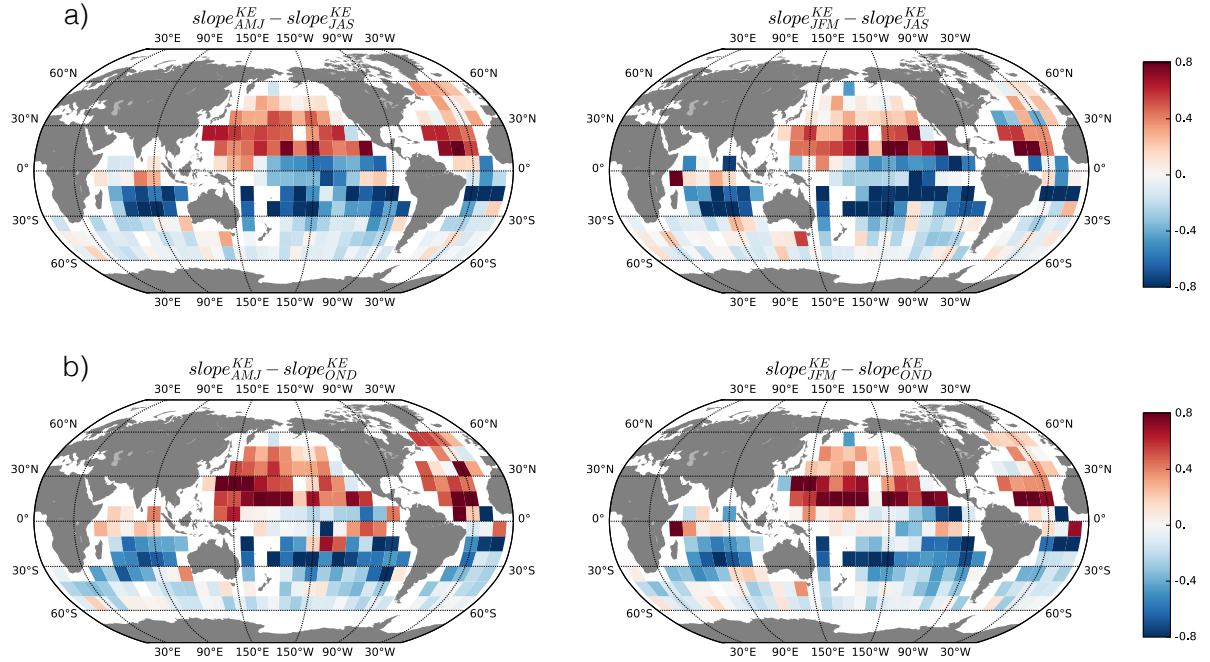


Figure 4: Difference of spectral slopes of KE compared to (a) summer (left: $AMJ - JAS$, right: $JFM - JAS$) and (b) autumn (left: $AMJ - OND$, right: $JFM - OND$) at scales above 200km (5×10^{-3} cpkm).

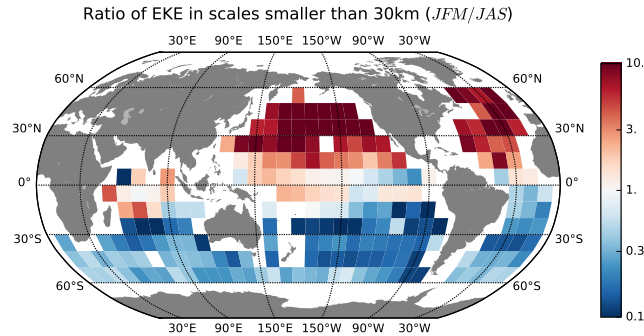


Figure 5: Ratio of EKE in scales smaller than 30km (3.3×10^{-2} cpkm) (EKE_{JFM}/EKE_{JAS}).

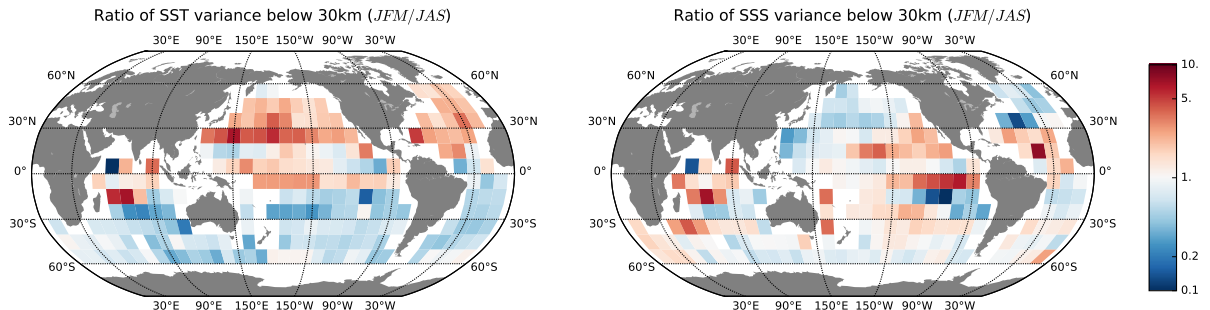


Figure 6: Ratio of SST (left) and SSS (right) variance in scales smaller than 30km (3.3×10^{-2} cpkm).

170 **4 . Discussion of Mechanisms Driving Seasonality**

171 *4 .1. Velocity field (EKE)*

172 Several different mechanisms have been proposed to generate seasonality in upper-ocean
173 meso- and submesoscale turbulent kinetic energy as summarized in the introduction. The emer-
174 gence of seasonality in this relatively coarse-resolution model provides an opportunity to test
175 how seasonality is reproduced in a GCM among the four hypotheses. Below we examine the
176 evidence for each mechanism using the available model output.

177 *4 .1.1. Variation in BCI*

178 Baroclinic instability transfers available potential energy (APE) into eddy kinetic energy
179 (EKE), generally at the scale of the most linearly unstable mode (*Gill et al.*, 1974). For fully
180 developed nonlinear turbulence, this transfer can be calculated from eddy correlation terms in
181 spectral space (e.g. *Holland*, 1978; *Sasaki et al.*, 2014). The necessary high-frequency 3D out-
182 put was unfortunately not saved from the POP simulation. However, *Qiu et al.* (2014) showed
183 that the temporal variations in finite-amplitude baroclinic conversion were well captured by
184 variations in linear BCI. Since linear BCI can be calculated from the mean hydrographic state,
185 we use it here as a proxy for baroclinic energy conversion. In addition, the linear analysis
186 provides valuable insights into the temporal scales, spatial scales, and the vertical structure of
187 instabilities.

188 We first calculate the growth rates of linear instabilities numerically using the same ap-
189 proach as *Smith* (2007). This method solves the linear quasigeostrophic (QG) eigenvalue prob-
190 lem using the local profile of geostrophic shear and stratification (N^2) at each point in the
191 horizontal to define the background state. While *Smith* (2007) considered just the annual mean
192 climatology, here we use a seasonally resolved climatology, revealing how instability varies
193 between winter and summer.

194 The background state was defined by taking the seasonal climatology over 41 years of
195 model output and aggregating the original 0.1° resolution to 1° . It is instructive to consider
196 the winter and summer climatological profiles of geostrophic velocity and N^2 , as shown in
197 Fig. 7 (a), an example from the Kuriosio region. While there are some seasonal difference in

198 geostrophic velocity and associated shear, the dominant seasonal change is in the upper ocean
199 N^2 , which is nearly 100 times weaker in the winter profile. This weak winter stratification
200 reflects the cumulative impact of deeper winter mixed layers. The winter N^2 profile can be
201 viewed as a superposition of interannual and intra-seasonal ML depth variability over the averag-
202 ing period. It is, however, problematic to attempt to define an actual mixed-layer depth from the
203 climatological profile; because mixed-layer depth identification (e.g. using a density threshold
204 criterion) is a nonlinear operation, the average of the mixed-layer depth is not the same as the
205 mixed-layer depth of the average. For this reason, we define the ML as the depth over which
206 N^2 experiences significant seasonality (approx. 160 m in Fig. 7 (a)). ML corresponds roughly
207 with the maximum winter mixed layer depth over the averaging interval.

208 The growth rates of the linear instabilities were determined numerically using the `oceanmodes`
209 python package¹ developed for this study (hereon we will refer to this as the numerical solu-
210 tion). The numerical details of the linear stability calculation are given in Appendix A.5; here
211 we show only the final results. The growth rates for the same Kuroshio example region are
212 shown in Fig. 7 (c) as a function of zonal wavenumber. (In the example, meridional wavenum-
213 ber is set to zero, but full two-dimensional stability calculations were also performed.) This
214 figure also shows several relevant length scales: the full-depth Rossby radius R_d , the mixed-
215 layer (ML) Rossby radius R_d^{ML} , and the model Nyquist wavelength (defined as two grid points
216 $2\Delta x$). R_d was calculated numerically with the `oceanmodes` package using the seasonal
217 climatology of N^2 (buoyancy frequency), while R_d^{ML} was derived from the depth averaged
218 buoyancy frequency over the mixed layer (i.e. $R_d^{ML} = \overline{N^{zML}} H_{ML}(\pi f)^{-1}$).

219 We observe large differences between winter and summer numerical growth rates, espe-
220 cially at small scales. Most of the small scale instability predicted cannot be resolved by the
221 model since it occurs at smaller scales than the model grid scale (thick black line in Fig. 7 (c)).
222 However, there is still a large seasonal difference in the resolved growth rates around the model
223 Nyquist wavelength. The vertical structure of the mode with a local maximum growth rate
224 around the Nyquist wavelength, shown in Fig. 7 (b), is strongly surface intensified. This is

¹This open source package is available at <https://github.com/rabernat/oceanmodes>. Appendix A.5.

225 the smallest instability that can potentially be resolved, although its growth is likely strongly
226 damped by numerical dissipation.

227 To quantify the contribution of the reduced near-surface stratification during winter to the
228 growth rates, we artificially homogenize the stratification during winter in the ML to the value
229 at the base of ML and then recalculate the numerical growth rate, leaving the geostrophic
230 velocity profiles untouched. The blue dotted line in Fig. 7 (c) shows the growth rate (σ_{JFM}^{ML}) for
231 this N^2 profile. We see that the large growth rates at small scales disappear, while the growth
232 rates near the full-depth deformation radius remain unchanged. This experiment reveals that
233 the main driver of seasonality in growth rates is indeed the weak near-surface stratification in
234 winter. Furthermore, the lack of significant seasonal changes in deep shear/stratification and
235 corresponding large-scale growth rates indicates that deep BCI is unlikely to be the main driver
236 of seasonality. This general behavior holds for all the seven example regions (not shown).

237 The importance of weak upper ocean stratification in driving seasonality in instability is
238 qualitatively consistent with the MLI mechanism (Boccaletti *et al.*, 2007; Callies and Ferrari,
239 2013; Callies *et al.*, 2016). To test the quantitative connection to MLI theory, we compare the
240 full growth rates to the approximated baroclinic instability models of Eady (1949) (Fig. 7 (c)),
241 which is considered to be a good approximation for MLI (Boccaletti *et al.*, 2007). The ana-
242 lytical Eady growth rates were calculated using the three different assumptions for the Rossby
243 deformation radius. (Due to how ML depth was defined, ML Eady estimates have only been
244 given for winter.) We find that the ML Eady growth rates during winter are a good proxy for
245 the full numerical solution in the Kuroshio region, capturing roughly the scale and magnitude
246 of the dominant peak (although the numerical solutions contain even smaller-scale instabilities)
247 ². Since the ML depth is related to the maximum winter ML depth, it is not surprising that the
248 ML Eady and ML Rossby wavelength $L_d^{ML} (\equiv 2\pi R_d^{ML})$ capture the scales and large growth
249 rates of this mode of instability. Examination of all seven example regions revealed that the

²Unsurprisingly, the (full-depth) Eady solutions using R_d do not provide a very good fit to the numerical solution as it is difficult to assume that the stratification is uniform over the whole depth (Fig. 7 (c)). The Stone growth rate and wavenumber scale (Stone, 1972) used in Boccaletti *et al.* (2007) did not agree well with the numerical solution of linear stability (not shown). The small wavenumbers in the Stone setup were solely due to the large Richardson number in the upper layer in the POP simulation, which can be on the order of $O(10^2)$, unlike in Boccaletti *et al.* (2007) where the Richardson number was taken to be $O(1)$. Henceforth, we will not further consider the Eady and Stone growth rate.

250 ML Eady model qualitatively captures the dominant mode of baroclinic instability around the
 251 Nyquist wavelength during winter in eddy active regions (not shown).

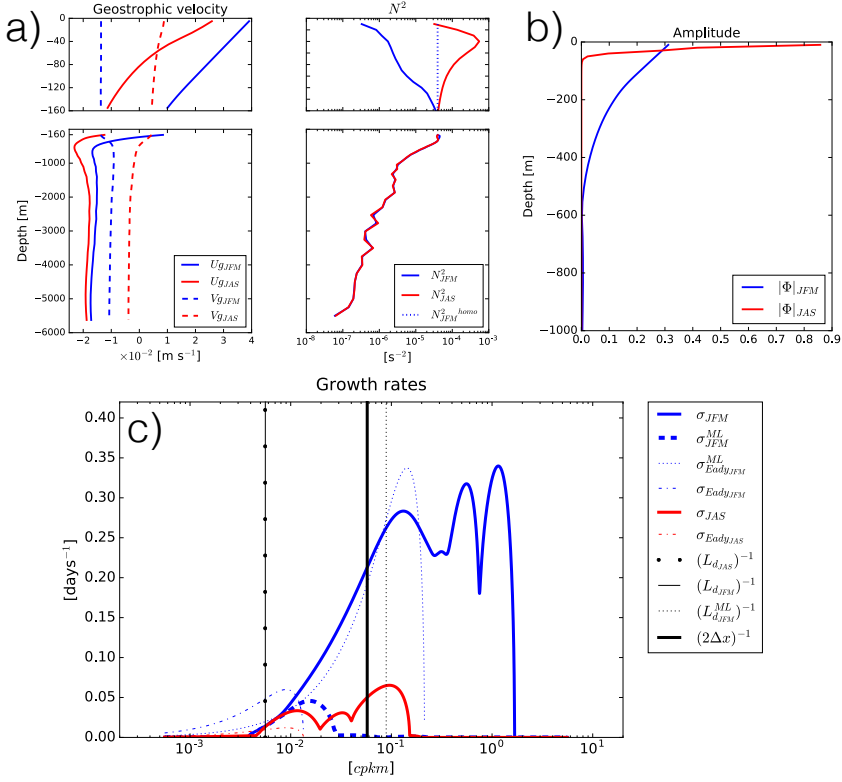


Figure 7: (a) The geostrophic velocity and buoyancy frequency. We also show the homogenized buoyancy frequency in the ML for winter and summer. The figure is divided at the ML base. (b) amplitude of the unstable mode with the largest growth rate closest to the Nyquist wavenumber. (c) Numerical solution of growth rates in the Kuroshio region for each season plotted against the zonal inverse wavelength with zero meridional wavenumber: linear instability solved with original profile (solid line) and with homogenized stratification in the ML (dashed line). The Eady (dot-dashed line) and ML Eady (dotted line) growth rate are shown as well. The zonal inverse wavelength was defined between the range of $10^{-1} \sim 10^3 L_d^{-1}$. The Rossby deformation inverse wavelength are shown in black thin lines and the thick black line indicates the Nyquist wavelength.

252 We now assess the seasonality in linear instability at the global scale. In Fig. 8, we show the
 253 seasonal difference of the maximum numerical growth rates at the Nyquist wavelength. (The
 254 maximum was taken from the two-dimensional zonal/meridional-wavenumber space.) We see
 255 that the maximum growth rates are consistently larger during winter than summer, coherent
 256 with the seasonal pattern of EKE spectra, consistent with the example region examined above.

257 If MLI is indeed the driver of the seasonal variations seen in the KE spectra, the unstable
 258 mixed-layer modes must be resolved by the model grid. The 0.1° resolution of the POP model
 259 is very fine for a climate model, but it is still even not classified as mesoscale resolving at high

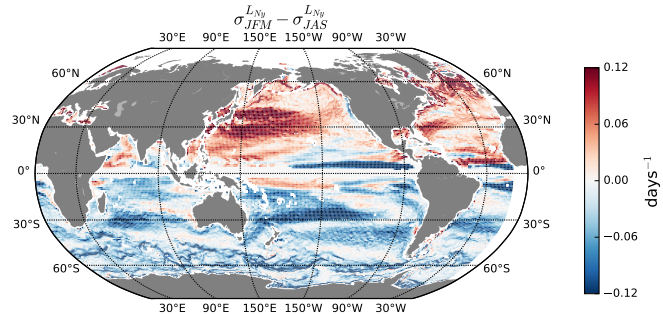


Figure 8: Seasonal variation of the maximum growth rate solved numerically over a polar coordinate at the Nyquist wavelength.

latitudes (Hallberg, 2013)³. We argued above that the growth rate at small scales is due to MLI, with a peak at roughly the mixed layer deformation scale L_d^{ML} . The degree to which this is resolved at a particular location depends, then, on how L_d^{ML} varies with grid resolution, or Nyquist wavelength $2\Delta x$. In Fig. 7, we showed that the large growth rates around the Nyquist wavelength are due to the instability around L_d^{ML} . In Fig. 9, we plot the zonal average of R_d and R_d^{ML} , and the ratio of this wavelength to the model Nyquist wavelength in winter and summer. The ratio varies from near 0.1 at low latitudes to 10 at high latitudes. Note also that in Fig. 7, the growth rate increases strongly with wavenumber near the model grid scale, implying that, even if L_d^{ML} is not resolved, the most unstable resolved instability will still be near the grid scale.

All of the discussion above shows that there is a strong seasonality signal in MLI, and that the instability can plausibly be resolved by the model. To test the connection between the seasonality in the spectra and MLI globally, we show the correlation between the seasonal anomaly in small-scale EKE and the numerical growth rate at the Nyquist wavelength in Fig. 10. The scatter plot shows significant correlation in latitudes higher than 20° , supporting the hypothesis that the seasonality seen in Fig. 4 and 5 is due to MLI. Although towards the poles the spatial scale where the MLI is the largest becomes smaller than the POP simulation resolution (Fig. 9), it appears that as long as the spatial scales of MLI are on the same order of the grid scale, MLI will be partially resolved.

³ Note that Hallberg (2013) classifies a model as mesoscale resolving if it resolves the deformation radius R_d of the first internal mode with at least two grid points. The most unstable mode of the linear instability occurs at $L_d^{ML} = 2\pi R_d^{ML} \simeq 6R_d^{ML}$. This is significantly larger than R_d^{ML} itself.

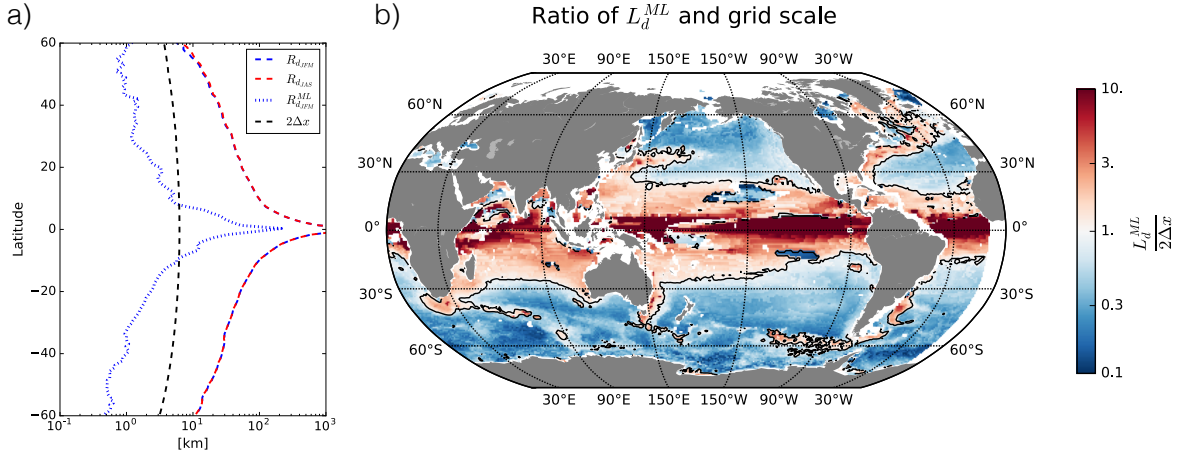


Figure 9: (a) The the zonal average of the Rossby radius (R_d) for winter and summer and the MLX Rossby radius (R_d^{ML}) for winter. The black dashed line indicates the Nyquist wavelength. (b) Ratio of the Rossby wavelength calculated over the mixing layer to the Nyquist wavelength ($L_d^{ML}(2\Delta x)^{-1}$). The values of L_d^{ML} used in the northern hemisphere are values during JFM (boreal winter) and JAS (austral winter) for the southern hemisphere. The black contours indicate where the ratio is unity.

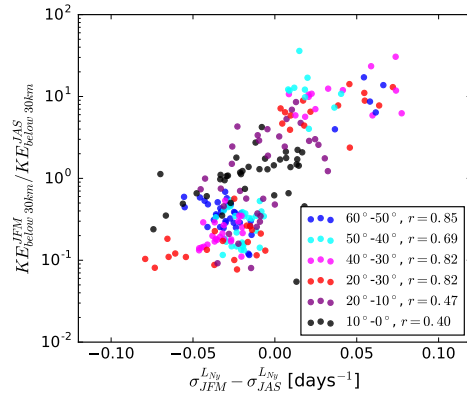


Figure 10: Scatter plot of seasonal difference in EKE against the seasonality in maximum growth rate of the numerical solution at the Nyquist wavelength. The correlations are shown for each latitudinal band.

279 The KE spectra (Fig. 3) also show weak seasonal variations at larger scales. The energy
 280 in the smallest scales peaks in winter, while the energy in the lower mesoscale range (between
 281 50km and 100km, i.e. $10^{-2} - 2 \times 10^{-2}$ cpkm) peaks in spring. The spectral slopes (Fig. 4) are
 282 consistent with this variability as well: spring and autumn having the shallowest and steepest
 283 slopes at scales above 200km (5×10^{-1} cpkm). *Qiu et al.* (2014) argued that seasonality in
 284 submesoscale energy cascades upscale, with a time lag, to induce seasonality in the mesoscale.
 285 In this mechanism, during winter time, deeper ML and reduced stratification lead to enhanced
 286 MLI (*Boccaletti et al.*, 2007; *Fox-Kemper et al.*, 2008), which becomes an energy source dur-
 287 ing wintertime at the smallest scales. This excess energy cascades inversely and reaches the

mesoscale in the springtime. To test whether this is a plausible explanation for the POP model mesoscale seasonality, we can quantify the time-lag in the inverse energy cascade via the eddy turnover timescale. The eddy turnover timescale quantifies the rate at which energy is transferred across scales via nonlinear eddy-eddy interaction. It is defined as

$$\tau_k = \frac{k^{-1}}{v_k} = [k^3 \mathcal{E}(k)]^{-1/2} \quad (1)$$

(e.g. *Vallis*, 2006) where k , v_k , and $\mathcal{E}(k)$ are the wavenumber, eddy velocity associated the wavenumber and the EKE spectrum respectively. τ_k can be considered as the approximate timescale of the spectral energy transfer. As shown in Fig. 11, we obtain values of 40-50 days in the inertial range and 100 days for regions with low eddy activity (not shown). These timescales are consistent with the mechanism of *Qiu et al.* (2014) and suggest that the EKE spectra (Fig. 3) may reflect a time-lagged cascade of submesoscale energy to larger scales.

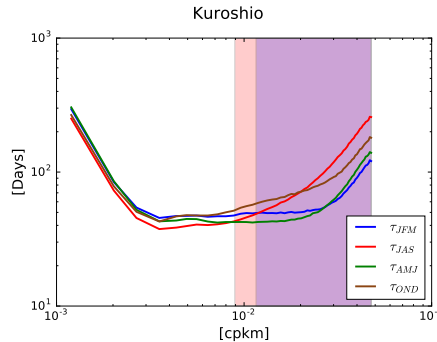


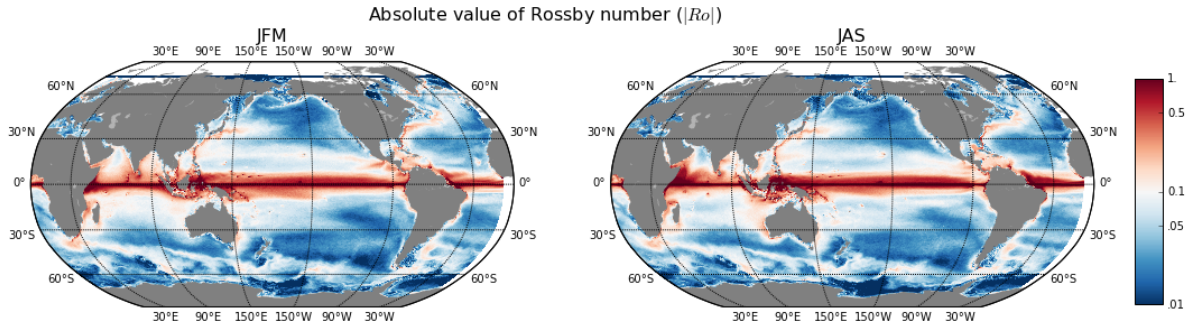
Figure 11: Eddy turnover timescale in days for the Kuroshio region in Fig. 1. The color shadings represent the EKE dissipation range for JFM (blue) and JAS (red).

297

298 4.1.2. Variation in frontogenesis

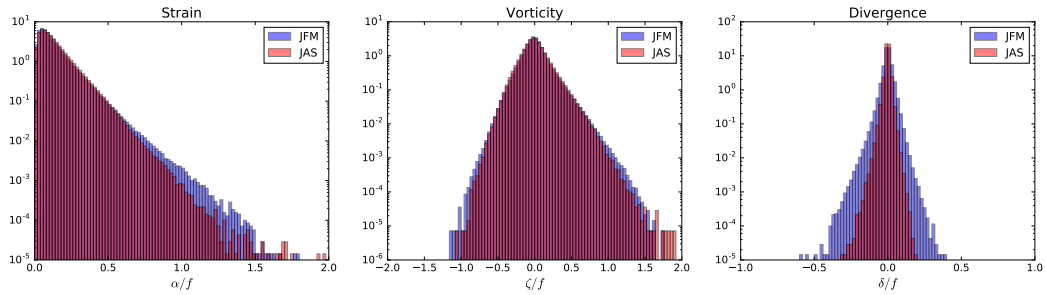
Another proposed mechanism for generating submesoscale energy is frontogenesis (FG) due to mesoscale straining (*Mensa et al.*, 2013; *McWilliams*, 2016). For FG to occur, the Rossby number ($Ro = \overline{|\zeta|}^t / f$, where $\overline{|\zeta|}^t$ is the time average of the absolute values of relative vorticity during each season) needs to be on the order of unity, i.e. $|Ro| \sim O(1)$ (*Mahadevan and Tandon*, 2006). In the POP simulations, in both seasons, $|Ro|$ is an order smaller across the globe except for the equatorial regions where the Coriolis parameter becomes zero. There is also no significant seasonality in $|Ro|$ (Fig. 12). This fortifies our argument that the dominant

306 factor for seasonality we see in the POP simulation is MLI. There may still be FG at work at
 low Ro , but the model is unlikely to fully resolve the buoyancy-front sharpening processes.



307 Figure 12: Global pattern of Rossby number at the surface for each season (left: JFM, right: JAS).

308 Another way at looking at the relevance of strain-induced FG (*McWilliams*, 2016) in our
 309 study is whether there is significant seasonality in the strain ($\alpha = [(\frac{\partial u}{\partial x} - \frac{\partial v}{\partial y})^2 + (\frac{\partial v}{\partial x} + \frac{\partial u}{\partial y})^2]^{1/2}$)
 310 field. Figure 13 plots the the histogram of strain, relative vorticity and divergence. It shows
 311 that although there is seasonality in the strain field normalized by the Coriolis parameter, the
 312 difference is very small (the y-axis in the histogram is in log scale) and this is case for all seven
 313 regions (not shown) in Fig. 1, consistent with Fig. 12. It is, however, likely that MLI and FG
 occur simultaneously and reinforce each other, making it difficult to rule FG out completely.



314 Figure 13: Histogram of the strain in the Kuroshio region shown in Fig. 1. The y-axis is in a log scale to
 emphasize the seasonality.

315 4.1.3. Variation in gravity wave energy

316 In a recent study *Rocha et al.* (2016b) attribute some seasonality, particularly during sum-
 317 mer time, to the interaction between internal tide and inertia-gravity waves, which the POP
 318 simulation does not resolve (*Small et al.*, 2014). Hence, it is unlikely that the seasonality we
 319 see in the POP simulation to be caused by internal waves. We have quantified this by calculat-
 320 ing the rotational and divergent spectra (*Callies and Ferrari*, 2013; *Bühler et al.*, 2014; *Rocha*

321 *et al.*, 2016a) in the same seven regions where we did the linear stability analysis. An arbitrary flow field can be decomposed into the rotational (ψ) and divergent (ϕ) components. The decomposed spectra indicates the energy contained in each component (ψ, ϕ) respectively. Internal gravity waves are divergent by nature in a 2D sense, and the divergent spectrum indicates the kinetic energy contained in internal gravity waves.

326 Figure 3 and 14 show that for all regions, the rotational component dominates for both seasons and therefore, the seasonality seen in the POP simulation is mostly due to the rotational component of the velocity field, i.e. geostrophic turbulence, which is non-divergent to its first order.

330 4 .2. SST and SSS

331 As shown in Figs. 3 and 6, SST and SSS wavenumber spectra undergo a broadband seasonal cycle with little change in spectral slope. In principle, the tracer spectral variance budget could be used to assess the cause of the SST and SSS seasonality. Unfortunately, the available model output is not sufficient to form a closed spectral variance budget. Further analysis of SST and SSS spectral seasonality will be addressed in a future study using a regional submesoscale resolving numerical model.

337 5 . Conclusions

338 We have assessed the seasonality in ocean surface wavenumber spectra in the (sub)mesoscale wavelength range from the the ocean component of a global climate model. Although this model is not submesoscale resolving, we found a clear signature of seasonally varying mixed-layer baroclinic instability. The KE fields showed clear seasonal difference in both the slopes and power level. For SST, spectral slopes did not vary in a uniform way, but the variance below 30km (3.3×10^{-2} cpkm) was higher during boreal (austral) winter in the northern (southern) hemisphere. The results for SSS were surprising in a sense that is showed the opposite signal for seasonality; higher variance during boreal (austral) summer in the northern (southern) hemisphere.

347 In terms of the actual values of the spectral slopes, it was difficult to extract physical meanings and compare them to turbulent inertial range predictions because the subgrid diffusion

349 impacted the spectra over a wide range of wavenumbers. We, therefore, have only shown the
350 seasonal difference of spectral slopes at the largest scales above 200km (5×10^{-3} cpkm), and
351 energy and variance below scales of 30km (3.3×10^{-2} cpkm); spring (autumn) time had the
352 shallowest (steepest) slopes and wintertime had the highest energy at the smallest scales.

353 There have been four major hypotheses proposed in explaining seasonality in mesoscale
354 turbulence; (i) variation in the interior baroclinic instability (BCI) due to seasonality in the ver-
355 tical shear of the full-depth background state (Qiu *et al.*, 2014), (ii) variation in the mixed-layer
356 BCI (MLI) due to seasonality in ML stratification, depth and vertical shear in the mixed layer
357 (Boccaletti *et al.*, 2007; Qiu *et al.*, 2014; Callies *et al.*, 2016), (iii) variation in frontogenesis
358 due to seasonality in lateral strain and convergence in the density horizontal gradients (Mensa
359 *et al.*, 2013) and (iv) variation in internal gravity waves due to seasonality in re-stratification of
360 the upper ocean (Rocha *et al.*, 2016b).

361 In our study using the POP simulation, we have shown that the seasonality seen in the
362 KE field is dominantly due to MLI, which can be approximated by the ML Eady model in
363 eddy active regions (e.g. Callies and Ferrari, 2013). When the ML depth is deeper during
364 wintertime, available potential energy for BCI increases. This energizes the entire mixed layer
365 and, subsequently, the submesoscale range through non-linear interactions among scales in
366 turbulence (Callies *et al.*, 2015; Brannigan *et al.*, 2015). Since the grid scale of the POP
367 simulation is on the same order of the length scale at which the growth rate of MLI is largest,
368 MLI is at least partially resolved in the POP simulation. Due to the inverse cascade, energy is
369 transported from submesoscale to mesoscale, which is likely what is seen in the wavenumber
370 spectra. Qiu *et al.* (2014) showed a time-lag in the energy to cascade upscale, and our results
371 are consistent with their finding; winter has the highest energy at the smallest scales, spring
372 and autumn spectra have the highest and lowest energy respectively in the range of 50-100km
373 ($10^{-2} - 5 \times 10^{-2}$ cpkm) and summertime has the highest energy at the largest scales.

374 The POP simulation has the spatial resolution of 0.1° in latitude and longitude. Due to
375 the subgrid diffusion, however, the effective spatial resolution is much coarser, so it is not sur-
376 prising if our results have underrepresented the submesoscale features. Nevertheless, we have
377 shown MLI being the dominant cause for seasonality in the modeled ocean mesoscale turbu-

378 lence. We also emphasize that although there have been studies in idealized models (*Boccaletti*
379 *et al.*, 2007; *Fox-Kemper et al.*, 2008; *Fox-Kemper and Ferrari*, 2008; *Brannigan et al.*, 2015;
380 *Callies et al.*, 2016) and specific regions (*Qiu et al.*, 2014; *Callies et al.*, 2015), this is the
381 first study to look at MLI on a global scale. The presence of clear seasonality signals at 30km
382 (3.3×10^{-2} cpkm) and below in every ocean basin implies a robust mechanism for seasonal-
383 ity despite the limited resolution of the model. The implications of this seasonality for air-sea
384 interaction, ocean ecosystems, and eddy fluxes is an important question for future research.

385 *Acknowledgements* This research was supported by NASA Award NNX16AJ35G. Aber-
386 nathey acknowledges additional support from NSF Award OCE-1553593. Uchida acknowl-
387 edges additional support from the Heiwa Nakajima Foundation. We thank Frank Bryan and
388 Justin Small for sharing the CESM simulation outputs. Data was accessed via the Yellowstone
389 computing system (ark:/85065/d7wd3xhc), provided by NCAR’s Computational and Informa-
390 tion Systems Laboratory, sponsored by the National Science Foundation.

391 Appendix

392 A .1. Isotropic wavenumber spectra besides the Kuroshio, Gulf Stream and ACC region

393 Figure 14 shows the isotropic wavenumber spectra of EKE, SST and SSS for regions other
394 than the ones shown in Fig. 3 for each season. The EKE spectra is decomposed into the rota-
395 tional and divergent component.

396 A .2. Method for Deriving Isotropic Spectra

We will show the normalization factor of an isotropic wavenumber spectra (B), which arises from the Plancherel theorem, i.e. the variance of an arbitrary isotropic variable is the same in the spatial and wavenumber domain:

$$\overline{\theta^2}^{xy} = \int_0^\infty B(K) dK$$

397 where the arbitrary variable θ has the dimension D .

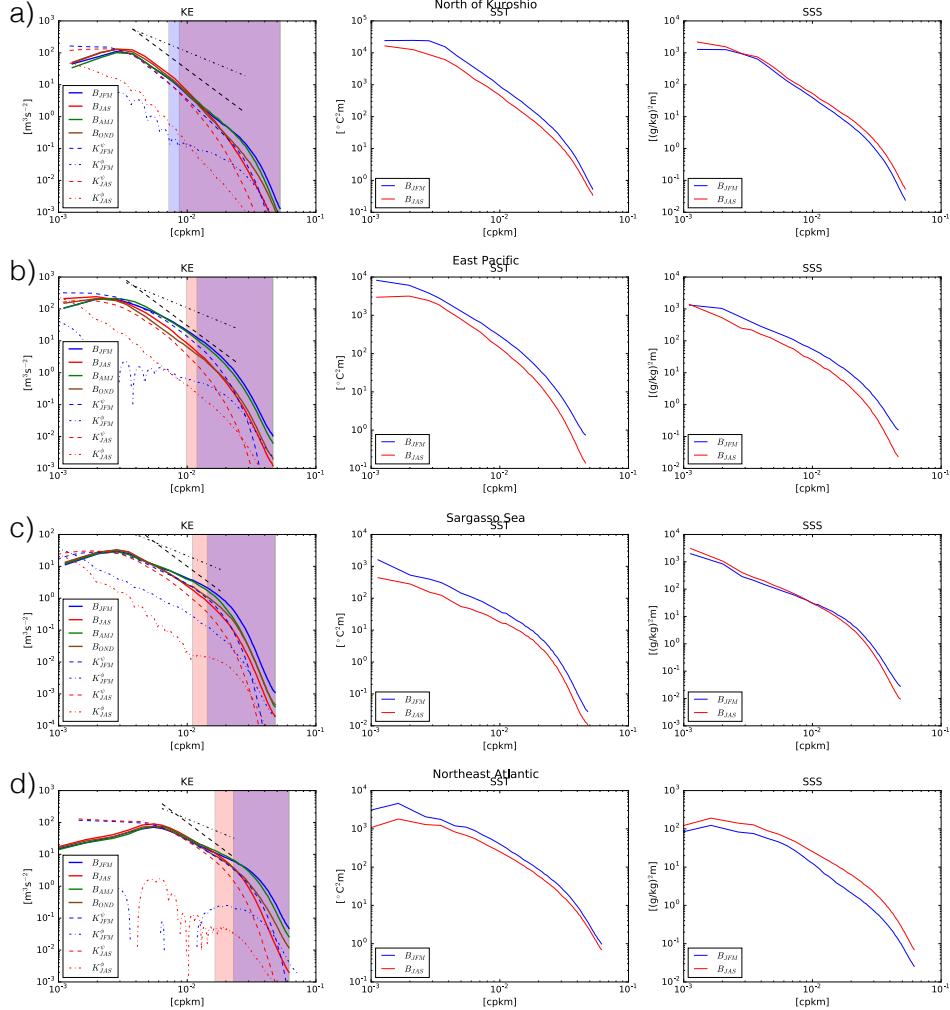


Figure 14: Seasonally-averaged spectra in: (a) north of Kuroshio, (b) east Pacific, (c) Sargasso Sea, and (d) northeast Atlantic. The shading shows the dissipation range defined as where 80% of the dissipation due to biharmonic diffusion occurs and the black dashed and dotted lines show the spectral slope of -3 and -5/3 respectively.

The domain-averaged variance for a 2D field is

$$\overline{\theta^2}^{xy} = \frac{1}{XY} \int_{-\infty}^{\infty} \int_{-\infty}^{\infty} \theta^2(x, y) dx dy \quad [D^2]$$

and the Fourier pairs are

$$\theta(x, y) = \int_{-\infty}^{\infty} \int_{-\infty}^{\infty} \hat{\theta}(k, l) e^{2\pi i(kx+ly)} dk dl$$

$$\begin{aligned}
\hat{\theta}(k, l) &= \int_{-\infty}^{\infty} \int_{-\infty}^{\infty} \theta(x, y) e^{-2\pi i(kx+ly)} dx dy \\
&\approx \Delta x \Delta y \sum_p \sum_q \theta(x_p, y_q) e^{-2\pi i(kx_p+ly_q)} \\
&\equiv \Delta x \Delta y \tilde{\theta}(k, l) [D m^2]
\end{aligned}$$

where $\hat{\theta}$ [$D m^2$] and $\tilde{\theta}$ [D]. The Plancherel theorem still looks the same

$$\int_{-\infty}^{\infty} \int_{-\infty}^{\infty} \theta(x, y)^2 dx dy = \int_{-\infty}^{\infty} \int_{-\infty}^{\infty} |\hat{\theta}(k, l)|^2 dk dl$$

and writing out the right-hand side (RHS) in a discrete form

$$\begin{aligned}
\Delta x \Delta y \sum_p \sum_q \theta(x_p, y_q)^2 &\approx \int_{-\infty}^{\infty} \int_{-\infty}^{\infty} \theta(x, y)^2 dx dy \\
&= \int_{-\infty}^{\infty} \int_{-\infty}^{\infty} |\hat{\theta}(k, l)|^2 dk dl \\
&\approx \Delta k \Delta l \sum_m \sum_n |\hat{\theta}(k_m, l_n)|^2 \\
&= \Delta k \Delta l (\Delta x \Delta y)^2 \sum_m \sum_n |\tilde{\theta}(k_m, l_n)|^2
\end{aligned}$$

The inverse wavelengths are defined as

$$k \equiv \frac{(-\frac{N_x}{2}, \dots, -1, 0, 1, \dots, \frac{N_x}{2} - 1)}{N_x \Delta x}$$

hence,

$$\Delta x \Delta y \sum_p \sum_q \theta(x_p, y_q)^2 = \frac{1}{N_x^2 N_y^2 \Delta k \Delta l} \sum_m \sum_n |\tilde{\theta}(k_m, l_n)|^2$$

³⁹⁸ Now, defining the normalized discrete Fourier coefficients as

$$\check{\theta}(k_m, l_n) \equiv \frac{1}{N_x N_y \sqrt{\Delta k \Delta l}} \tilde{\theta}(k_m, l_n) [D m] \quad (\text{A-1})$$

the Plancherel theorem becomes

$$\Delta x \Delta y \sum_p \sum_q \theta(x_p, y_q)^2 = \sum_m \sum_n |\check{\theta}(k_m, l_n)|^2$$

The isotropic PSD, however, needs to be defined carefully and due to transformation to polar coordinates, we pick up an extra factor of k_r in the integral, i.e. in order to satisfy Webb's condition in 2D, we need

$$\begin{aligned} \int_0^\infty \int_{-\pi}^\pi B(k_r, \phi) d\phi dk_r &= \langle \theta^2 \rangle = \frac{1}{A} \int_A \left(|\hat{\theta}(k_r, \phi)|^2 k_r d\phi \right) dk_r \\ &\approx \frac{1}{\pi R^2} \int_0^R \left(\int_{-\pi}^\pi |\hat{\theta}(k_r, \phi)|^2 k_r d\phi \right) dk_r \quad [D^2] \\ \therefore \int_{-\pi}^\pi B_{2D}(k_r, \phi) d\phi &= \frac{1}{\pi R^2} \int_{-\pi}^\pi |\hat{\theta}(k_r, \phi)|^2 k_r d\phi \quad [D^2 m] \end{aligned}$$

where $\Delta k_r \equiv \frac{1}{N_r \Delta r}$. For a isotropic field, this reduces to

$$\overline{\theta^2}^{xy} = \int_0^\infty B_{2D}(k_r) dk_r = \sum_n B_{2D}(k_{rn}) \Delta k_r = (\Delta k_r)^3 \sum_n \frac{k_{rn}}{\pi} |\hat{\theta}(k_{rn})|^2 \quad [D^2]$$

Using the results above, the relation between the Cartesian and polar coordinate for the Fourier components are

$$\begin{aligned} |\hat{\theta}(k_m, l_n)|^2 &= (N_x \Delta x)(N_y \Delta y) |\check{\theta}(k_m, l_n)|^2 \Leftrightarrow |\hat{\theta}(k_{rn}, \phi)|^2 = \pi (N_r \Delta r)^2 |\check{\theta}(k_{rn}, \phi)|^2 \\ &\Leftrightarrow |\hat{\theta}(k_{rn}, \phi)|^2 = \frac{\pi}{(\Delta k_r)^2} |\check{\theta}(k_{rn}, \phi)|^2 \quad [D^2] \end{aligned}$$

In an isotropic state

$$|\hat{\theta}(k_{rn})|^2 = \frac{\pi}{(\Delta k_r)^2} |\check{\theta}(k_{rn})|^2 \quad [D^2]$$

Hence the power-spectral density $B_{2D}(k_r)$ is

$$B_{2D}(k_{rn}) = k_{rn} \frac{(\Delta k_r)^2}{\pi} |\hat{\theta}(k_{rn})|^2 = k_{rn} |\check{\theta}(k_{rn})|^2 \quad [D^2 m]$$

We shall refer to *Menke and Menke* (2009). From the Plancherel theorem, we have

$$\begin{aligned} \Delta x \Delta y \sum_{p=0}^{N_x-1} \sum_{q=0}^{N_y-1} w^i(x_p, y_q) d^i(x_p, y_q) &\simeq \iint [w(x, y) d(x, y)^i]^2 dx dy \\ &= \iint |\hat{d}^i(k, l)|^2 dk dl \\ &\simeq \Delta k \Delta l \sum_{m=-N_x/2+1}^{N_x/2} \sum_{n=-N_y/2+1}^{N_y/2} |\hat{d}^i(k_m, l_n)|^2 \end{aligned}$$

where $w(x, y)$ and $d(x, y)$ are the tapering function and data respectively and \hat{d} includes the tapering. Using the relation shown in the Appendix A.2 yields

$$\Delta k \Delta l \sum_m^{N_x/2+1} \sum_n^{N_y/2+1} |\hat{d}^i(k_m, l_n)|^2 = \Delta k \Delta l (\Delta x \Delta y)^2 \sum_{m=-N_x/2+1}^{N_x/2} \sum_{n=-N_y/2+1}^{N_y/2} |\tilde{d}^i(k_m, l_n)|^2$$

so we get

$$\sum_p^{N_x} \sum_q^{N_y} (w^i(x_p, y_q) d^i(x_p, y_q))^2 = \frac{1}{N_x N_y} \sum_{m=-N_x/2+1}^{N_x/2} \sum_{n=-N_y/2+1}^{N_y/2} |\tilde{d}^i(k_m, l_n)|^2 \quad (*)$$

We can approximate the left-hand side (LHS) of the equation above as

$$\begin{aligned} (N_x N_y) \sum_p^{N_x} \sum_q^{N_y} (w^i(x_p, y_q) d^i(x_p, y_q))^2 &\sim \sum_p^{N_x} \sum_q^{N_y} w_{pq}^i {}^2 \sum_p^{N_x} \sum_q^{N_y} d_{pq}^i {}^2 \\ &= \frac{1}{N_x N_y} \sum_p^{N_x} \sum_q^{N_y} w_{pq}^i {}^2 (N_x N_y)^2 \frac{1}{N_x N_y} \sum_p^{N_x} \sum_q^{N_y} d_{pq}^i {}^2 \\ &= (N_x N_y)^2 f_T f_d \end{aligned}$$

where " \sim " means equivalent in a statistical sense and we have defined $f_T \equiv \frac{1}{N_x N_y} \sum_p^{N_x} \sum_q^{N_y} (w_{pq}^i)^2$, $f_d \equiv \frac{1}{N_x N_y} \sum_p^{N_x} \sum_q^{N_y} (d_{pq}^i)^2$. When no tapering is applied, the right-hand side (RHS) above becomes $(N_x N_y)^2 f_d$. The Plancherel relation (*) above becomes

$$f_T f_d \simeq \frac{1}{(N_x N_y)^2} \sum_{m=-N_x/2+1}^{N_x/2} \sum_{n=-N_y/2+1}^{N_y/2} |\tilde{d}^i(k_m, l_n)|^2 = \frac{1}{N_x N_y} \overline{|\tilde{d}^i|^2}$$

Since the mean of a χ^2 distribution is equivalent to the number of elements summed and the variance is twice the mean, we have $\overline{\phi^i}/c = 2$ or 1 and $\sigma_{\phi^i}^2/c^2 = 4$ or 2 where $\phi^i \equiv |\tilde{d}^i|^2$ and c is the normalization factor. Thus,

$$c = \frac{N_x N_y f_T f_d}{2} \quad (2 \leq i \leq N/2)$$

$$c = N_x N_y f_T f_d \quad (i = 1, N/2 + 1)$$

so $\phi^i/c (\equiv \Phi)$ follows the χ^2 distribution. Since, $\Phi(k_r)$ are normalized to the χ^2 distribution, the probability that the estimated spectrum $\Phi^{est}(k_{r_m})$ should be close to the true spectrum $\Phi^{true}(k_{r_m})$ is:

$$p\left(\frac{2\nu\Phi^{est}(k_{r_m})}{b} \leq \Phi^{true}(k_{r_m}) \leq \frac{2\nu\Phi^{est}(k_{r_m})}{a}\right) = 1 - \alpha$$

(*Gille (2015)*) where $1 - \alpha$ is the confidence level (i.e. $\alpha = 0.05$ for 95% confidence). a and b are the $(1 - \alpha)/2$ and $\alpha/2$ critical values of the $\chi^2(2\nu)$ distribution and ν ($\equiv NM(r)$) is the number of chunks that are added up. The $p\%$ confidence range therefore is:

$$\frac{2\nu}{b} \leq \frac{\Phi^{true}(k_{r_m})}{\Phi^{est}(k_{r_m})} \leq \frac{2\nu}{a}$$

Thus

$$\log(\Phi^{est}(k_{r_m})) + \log\left(\frac{2\nu}{b}\right) \leq \log(\Phi^{true}(k_{r_m})) \leq \log(\Phi^{est}(k_{r_m})) + \log\left(\frac{2\nu}{a}\right)$$

so the confidence interval is:

$$error_{high} = \log\left(\frac{2\nu}{a}\right), \quad error_{low} = \log\left(\frac{2\nu}{b}\right)$$

⁴⁰⁰ and to move the error bar around in the log-log dimension, we can multiply the values inside
⁴⁰¹ the logarithm by an arbitrary factor A .

402 *A .4. Dissipation range*

The biharmonic momentum dissipation terms are calculated as defined in the POP simulation,

$$D_H(u) = \nabla^2(A_M \nabla^2 u)$$

where

$$\begin{aligned} \nabla^2 u &= \Delta_x \delta_x \frac{\Delta_y \delta_x u}{UAREA} + \Delta_y \delta_y \frac{\Delta_x \delta_y u}{UAREA} \\ &\quad - u [\delta_x k_x - \delta_y k_y + 2(k_x^2 + k_y^2)] + 2k_y \delta_x v - 2k_x \delta_y v \end{aligned}$$

The coefficients k_x and k_y are the metric terms which arise when converting Cartesian coordinates to spherical coordinates. For further details of the definition of each variable, refer to *Smith et al.* (2010). We define the dissipation range the wavenumber above which 80% of the KE dissipation occurs, i.e.

$$0.8 = \frac{\int_{K_{diss}}^{K_{Ny}} [\check{u} \check{D}_H(u) + \check{v} \check{D}_H(v)] dK}{\int_{K_{min}}^{K_{Ny}} [\check{u} \check{D}_H(u) + \check{v} \check{D}_H(v)] dK}$$

403 where K_{Ny} , K_{min} , and K_{diss} are the Nyquist wavenumber, minimum wavenumber defined
 404 by the domain and the wavenumber which defines the dissipation range respectively. The $(\check{\cdot})$
 405 indicated the Fourier transforms defined in eqn. (A-1).

406 *A .5. Linear stability calculation*

The oceanmodes package solves the inviscid QG equations linearized around the mean background state ($u_g = -\frac{\partial \Psi}{\partial y}$, $v_g = \frac{\partial \Psi}{\partial x}$, N^2 , Q):

$$\frac{\partial q}{\partial t} + \mathbf{u}_g \cdot \nabla q + \mathbf{u} \cdot \nabla Q = 0$$

with the boundary condition of

$$\frac{\partial b}{\partial t} + \mathbf{u}_g \cdot \nabla b + \mathbf{u} \cdot \nabla (B + N^2 \eta) = 0$$

where a plane-wave solution for the perturbation, i.e. $\psi = \text{Re}[\Phi(z)e^{i(kx+ly-\omega t)}]$ is assumed and η is the topographic slope. The velocity field is divided into the geostrophic and perturbation component. The geostrophic velocity \mathbf{u}_g is derived as

$$\mathbf{u}_g = \frac{g}{f\rho_{ref}} [\bar{\rho} \mathbf{e}_z \times \nabla \eta + (\eta - z) \mathbf{e}_z \times \nabla \bar{\rho}]$$

where $\bar{\rho} \equiv \int_{-H}^0 \rho(z) dz$ and \mathbf{e}_z is the unit vector along the vertical axis. The reference density (ρ_{ref}) is taken to be the potential density at the surface.

$$q = \nabla^2 \psi + \Gamma \psi, \quad Q = \beta y + \Gamma \Psi$$

$$b = f \frac{\partial \psi}{\partial z}, \quad B = f \frac{\partial \Psi}{\partial z} \left(= \int N^2(z) dz \right)$$

are the perturbed and mean QG potential vorticity (QGPV) and buoyancy respectively where $\Gamma \equiv \frac{\partial}{\partial z} \left(\frac{f^2}{N^2} \frac{\partial}{\partial z} \right)$. The buoyancy frequency (N^2) was derived using the gsw Python package (<https://github.com/TEOS-10/python-gsw>).

Starting from the linearized QG potential vorticity equation around a state of rest ($\mathbf{u}_g = 0$) and prescribing a solution as $\Psi = \text{Re}[e^{i(kx+ly-\sigma t)}] \Phi(z)$, we get:

$$\begin{aligned} 0 &= \frac{\partial}{\partial t} \left[\nabla_z^2 \Psi + \frac{\partial}{\partial z} \left(\frac{f^2}{N^2} \frac{\partial \Psi}{\partial z} \right) \right] + \beta \frac{\partial \Psi}{\partial x} \\ &= i\sigma \left[(k^2 + l^2) e^{i(kx+ly-\sigma t)} \Phi - e^{i(kx+ly-\sigma t)} \frac{d}{dz} \left(\frac{f^2}{N^2} \frac{d\Phi}{dz} \right) \right] + ik e^{i(kx+ly-\sigma t)} \beta \Phi \end{aligned}$$

410

$$\Gamma \Phi \equiv \frac{d}{dz} \left(\frac{f^2}{N^2} \frac{d\Phi}{dz} \right) = - \left(k^2 + l^2 + \frac{k}{\sigma} \beta \right) \Phi \equiv -K^2 \Phi \quad (\text{A-2})$$

where K is defined as 2π over wavelength, which is often referred as "Rossby deformation wavenumber". Assuming the same conditions as in *Smith (2007)* and taking caution of the vertical layer setup in the POP model (Fig. 15), we can discretize the equation above as:

$$\Gamma_n^m \Phi_n = \frac{f^2}{\delta_n} \left(\frac{1}{{N_n}^2} \frac{\Phi_{n+1} - \Phi_n}{\Delta_n} - \frac{1}{{N_{n-1}}^2} \frac{\Phi_n - \Phi_{n-1}}{\Delta_{n-1}} \right) \quad (1 < n < \nu)$$

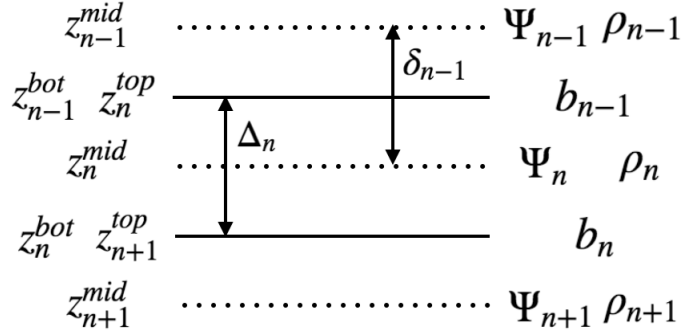


Figure 15: The vertical layer setup of the POP model. The stream function (Ψ) and density (ρ) are defined at the midpoint of each vertical layer and buoyancy (b, N) is defined on the boundaries of each layer.

$$\Gamma_1^m \Phi_1 = \frac{f^2}{\delta_1} \left(\frac{1}{{N_1}^2} \frac{\Phi_2 - \Phi_1}{\Delta_1} \right)$$

$$\Gamma_\nu^m \Phi_\nu = \frac{f^2}{\delta_\nu} \left(\frac{-1}{{N_{\nu-1}}^2} \frac{\Phi_\nu - \Phi_{\nu-1}}{\Delta_{\nu-1}} \right)$$

411 where the superscript m and subscript n ($= 1, 2, \dots, \nu$) represent the eigenmodes and vertical
 412 layer respectively. The Brunt-Vaisälä frequency (N) was derived using the Gibbs Seawater
 413 Oceanographic Toolbox (McDougall and Barker, 2011).

414 References

- 415 Boccaletti, G., R. Ferrari, and B. Fox-Kemper, Mixed layer instabilities and restratification,
 416 *Journal of Physical Oceanography*, 37, 2228–2250, 2007.
- 417 Brannigan, L., D. Marshall, A. Naveira-Garabato, and A. Nurser, The seasonal cycle of subme-
 418 soscale flows, *Ocean Modelling*, 2015.
- 419 Bühler, O., J. Callies, and R. Ferrari, Wave-vortex decomposition of one-dimensional ship-
 420 track data, *Journal of Fluid Mechanics*, 756, 1007, 2014.
- 421 Callies, J., and R. Ferrari, Interpreting energy and tracer spectra of upper-ocean turbulence in
 422 the submesoscale range (1–200 km), *Journal of Physical Oceanography*, 43, 2456–2474,
 423 2013.
- 424 Callies, J., R. Ferrari, J. Klymak, and J. Gula, Seasonality in submesoscale turbulence, *Nature
 425 communications*, 6, 2015.

- 426 Callies, J., G. Flierl, R. Ferrari, and B. Fox-Kemper, The role of mixed-layer instabilities in
427 submesoscale turbulence, *Journal of Fluid Mechanics*, 788, 5–41, 2016.
- 428 Capet, X., J. C. McWilliams, M. J. Molemaker, and A. F. Shchepetkin, Mesoscale to subme-
429 soscale transition in the California current system. part iii: Energy balance and flux, *Journal*
430 of *Physical Oceanography*, 38, 2256–2269, 2008.
- 431 Charney, J., Geostrophic turbulence, *Journal of the Atmospheric Sciences*, 28, 1087–1095,
432 1971.
- 433 Dong, C., J. McWilliams, Y. Liu, and D. Chen, Global heat and salt transports by eddy move-
434 ment, *Nature communications*, 5, 2014.
- 435 Eady, E. T., Long waves and cyclone waves, *Tellus*, 1, 33–52, 1949.
- 436 Fox-Kemper, B., and R. Ferrari, Parameterization of mixed layer eddies. part ii: Prognosis and
437 impact, *Journal of Physical Oceanography*, 38, 1166–1179, 2008.
- 438 Fox-Kemper, B., R. Ferrari, and R. Hallberg, Parameterization of mixed layer eddies. part i:
439 Theory and diagnosis, *Journal of Physical Oceanography*, 38, 1145–1165, 2008.
- 440 Gill, A., J. Green, and A. Simmons, Energy partition in the large-scale ocean circulation and
441 the production of mid-ocean eddies, in *Deep Sea Research and Oceanographic Abstracts*,
442 vol. 21, pp. 499–528, Elsevier, 1974.
- 443 Gille, S., Spectral uncertainties, <http://www-pord.ucsd.edu/~sgille/sio221c/lectures/spectra.pdf>,
444 2015.
- 445 Gula, J., M. J. Molemaker, and J. C. McWilliams, Submesoscale cold filaments in the gulf
446 stream, *Journal of Physical Oceanography*, 44, 2617–2643, 2014.
- 447 Hallberg, R., Using a resolution function to regulate parameterizations of oceanic mesoscale
448 eddy effects, *Ocean Modelling*, 72, 92–103, 2013.
- 449 Held, I., R. Pierrehumbert, S. Garner, and K. Swanson, Surface quasi-geostrophic dynamics,
450 *Journal of Fluid Mechanics*, 282, 1–20, 1995.

- 451 Holland, W. R., The role of mesoscale eddies in the general circulation of the ocean-numerical
452 experiments using a wind-driven quasi-geostrophic model, *Journal of Physical Oceanogra-*
453 *phy*, 8, 363–392, 1978.
- 454 Jayne, S., and J. Marotzke, The oceanic eddy heat transport*, *Journal of Physical Oceanogra-*
455 *phy*, 32, 3328–3345, 2002.
- 456 Lapeyre, G., and P. Klein, Dynamics of the upper oceanic layers in terms of surface quasi-
457 geostrophy theory, *Journal of physical oceanography*, 36, 165–176, 2006.
- 458 Large, W., J. McWilliams, S. Doney, et al., Oceanic vertical mixing: A review and a model with
459 a nonlocal boundary layer parameterization, *Reviews of Geophysics*, 32, 363–404, 1994.
- 460 Lévy, M., P. Klein, A. Tréguier, D. Iovino, G. Madec, S. Masson, and K. Takahashi, Modifica-
461 tions of gyre circulation by sub-mesoscale physics, *Ocean Modelling*, 34, 1–15, 2010.
- 462 Mahadevan, A., and A. Tandon, An analysis of mechanisms for submesoscale vertical motion
463 at ocean fronts, *Ocean Modelling*, 14, 241–256, 2006.
- 464 McCaffrey, K., B. Fox-Kemper, and G. Forget, Estimates of ocean macro-turbulence: structure
465 function and spectral slope from argo profiling floats, *Journal of Physical Oceanography*,
466 2015.
- 467 McClean, J., et al., A prototype two-decade fully coupled fine-resolution CCSM simulation,
468 *Ocean Modelling*, 39, 10–30, 2011.
- 469 McDougall, T., and P. Barker, Getting started with teos-10 and the gibbs seawater (gsw) oceano-
470 graphic toolbox, *SCOR/IAPSO WG*, 127, 1–28, 2011.
- 471 McWilliams, J. C., Submesoscale currents in the ocean, in *Proc. R. Soc. A*, vol. 472, p.
472 20160117, The Royal Society, 2016.
- 473 Menke, W., and J. Menke, *Environmental data analysis with MATLAB*, Elsevier, 2009.
- 474 Mensa, J., Z. Garraffo, A. Griffa, T. Özgökmen, A. Haza, and M. Veneziani, Seasonality of the
475 submesoscale dynamics in the gulf stream region, *Ocean Dynamics*, 63, 923–941, 2013.

- 476 Qiu, B., S. Chen, P. Klein, H. Sasaki, and Y. Sasai, Seasonal mesoscale and submesoscale eddy
477 variability along the north pacific subtropical countercurrent, *Journal of Physical Oceanog-*
478 *rphy*, 44, 3079–3098, 2014.
- 479 Rhines, P. B., Geostrophic turbulence, *Annual Review of Fluid Mechanics*, 11, 401–441, 1979.
- 480 Rocha, C. B., T. K. Chereskin, S. T. Gille, and D. Menemenlis, Mesoscale to submesoscale
481 wavenumber spectra in drake passage, *Journal of Physical Oceanography*, 46, 601–620,
482 2016a.
- 483 Rocha, C. B., T. K. Chereskin, S. T. Gille, and D. Menemenlis, Seasonality of submesoscale
484 dynamics in the kuroshio extension, *Geophysical Research Letters*, 2016b.
- 485 Sasaki, H., P. Klein, B. Qiu, and Y. Sasai, Impact of oceanic-scale interactions on the seasonal
486 modulation of ocean dynamics by the atmosphere, *Nature communications*, 5, 2014.
- 487 Small, R., et al., A new synoptic scale resolving global climate simulation using the community
488 earth system model, *Journal of Advances in Modeling Earth Systems*, 6, 1065–1094, 2014.
- 489 Smith, R., et al., The parallel ocean program reference manual, 2010.
- 490 Smith, S., The geography of linear baroclinic instability in earth’s oceans, *Journal of Marine*
491 *Research*, 65, 655–683, 2007.
- 492 Stammer, D., Global characteristics of ocean variability estimated from regional
493 topex/poseidon altimeter measurements, *Journal of Physical Oceanography*, 27, 1743–1769,
494 1997.
- 495 Stone, P. H., A simplified radiative-dynamical model for the static stability of rotating atmo-
496 spheres, *Journal of the Atmospheric Sciences*, 29, 405–418, 1972.
- 497 Thomas, L., A. Tandon, and A. Mahadevan, Submesoscale processes and dynamics, *Ocean*
498 *Modeling in an Eddying Regime*, *Geophys. Monogr. Ser.*, 177, 17–38, 2008.
- 499 Vallis, G. K., *Atmospheric and oceanic fluid dynamics: fundamentals and large-scale circula-*
500 *tion*, Cambridge University Press, 2006.

- 501 Volkov, D., T. Lee, and L. Fu, Eddy-induced meridional heat transport in the ocean, *Geophysical Research Letters*, 35, 2008.
- 502
- 503 Xu, Y., and L. Fu, Global variability of the wavenumber spectrum of oceanic mesoscale turbulence, *Journal of physical oceanography*, 41, 802–809, 2011.
- 504
- 505 Xu, Y., and L. Fu, The effects of altimeter instrument noise on the estimation of the wavenumber spectrum of sea surface height, *Journal of Physical Oceanography*, 42, 2229–2233, 2012.
- 506